

# Machine-Learning-Assisted Development of Carbon Steel With Superior Strength and Ductility Manufactured by Electron Beam Powder Bed Fusion



YUNWEI GUI, KENTA AOYAGI, HUAKANG BIAN, and AKIHIKO CHIBA

In this study, based on a novel support vector machine optimization method, a wide processing window for manufacturing defect-free S25C carbon steel by electron beam powder bed fusion (EB-PBF) was identified. Samples with same energy densities exhibited similar microstructures and mechanical properties. One sample showed an optimum strength and elongation combination of 459.3 MPa and 57.6 pct. The pearlite region with irregular cementite particles was the first to crack during deformation, and the cracks gradually expanded into the surrounding area. Ferrite, cellular structures, and pearlite with parallel and straight cementite particles could effectively modulate the deformation by slip and enhance the plasticity of the S25C parts. After quenching, the strength improved to an unprecedented value of 1722.5 MPa owing to the presence of martensite and dislocation entanglements, with an elongation of 16.8 pct. The strength decreased after further tempering, and the plasticity evidently increased, with an optimum strength and elongation combination of 722.7 MPa and 44.2 pct, respectively. The microstructure of tempered sample contained lath martensite, cementite particles, and sparse dislocation lines. These results demonstrate that the current method can serve as a powerful tool for effectively optimizing the high-dimensional parameters of the EB-PBF process to produce carbon steel with excellent mechanical properties.

<https://doi.org/10.1007/s11661-023-07251-1>  
© The Author(s) 2023

## I. INTRODUCTION

ADDITIVE manufacturing (AM) technology has distinct advantages over conventional manufacturing methods. It can be used to create 3D products through material deposition based on 3D computer-aided design data, offering operators the possibility of rapidly manufacturing complex-shaped or custom-made parts while reducing the number of processing steps and saving manufacturing time.<sup>[1-4]</sup> Electron beam powder-bed fusion (EB-PBF) is an important metal AM technique, in which powders are selectively melted with high-energy electron beams, thereby allowing for high degrees of

freedom in the formation of samples.<sup>[5]</sup> With the advantages of high energy utilization, high scanning speed, wide range of building temperatures, and high vacuum, EB-PBF allows not only the fabrication of high-quality products but also the control of their microstructures while avoiding oxidization and large thermal deformation. This makes the EB-PBF ideal for studying metallic materials.<sup>[6]</sup>

Steel is a workhorse material of our society and is used in many fields such as automobiles, maritime, and construction. Steel has the advantages of large reserves, and low production costs, and its microstructure and mechanical properties can be controlled by alloy element design and heat treatment.<sup>[7-9]</sup> Carbon steel mainly contains iron and carbon. Steel with a carbon content in the range of 0.22 to 0.28 mass pct is sold under the grade code S25C; it has a homogeneous microstructure and excellent machining properties. As carbon steel is being gradually employed in various new applications, simple shapes and structures have limited its further use, and it is necessary to find a method to fabricate carbon steel products with more complex structures and shapes and a higher performance. The EB-PBF and other AM methods have been increasingly used for developing high-performance materials; they are also widely used for steel materials, but mainly for alloy steels, such as stainless steel and tool steels, with few application

YUNWEI GUI is with the Department of Materials Processing, Graduate School of Engineering, Tohoku University, 6-6 Aramaki Aza Aoba, Aoba-ku, Sendai 980-8579, Japan and with the Institute for Materials Research, Tohoku University, 2-1-1 Katahira, Aoba-ku, Sendai 980-8577, Japan and also with the School of Materials Science and Engineering, University of Science and Technology Beijing, Beijing 100083, P.R. China. KENTA AOYAGI, HUAKANG BIAN, and AKIHIKO CHIBA are with the Institute for Materials Research, Tohoku University. Contact e-mail: kenta.aoyagi.e7@tohoku.ac.jp

Manuscript submitted June 4, 2023; accepted November 2, 2023.

Article published online November 16, 2023

examples for low-alloy and carbon steels.<sup>[10–14]</sup> Stainless steel and medium-carbon steels manufactured by selective laser melting (L-PBF) and directed energy deposition (L-DED) contain numerous cracks due to the thermal stresses generated during rapid solidification in the L-PBF or L-DED process, where no pretreatment is employed. These cracks lead to the accumulation of residual stresses in the material, resulting in warping, buckling, and internal cracking.<sup>[12,15,16]</sup> In the EB-PBF process, a preheating process is applied to effectively relieve the thermal stress of the powder bed, thus avoiding crack formation.<sup>[5,6,12,17]</sup>

However, the EB-PBF technology is associated with numerous and complex process parameters, because of which internal defects are easily generated when applied to carbon steel, which can significantly deteriorate its mechanical properties. To extend the application of the EB-PBF technology in the manufacturing of carbon steel, the issue of internal defects must be addressed. To date, most studies<sup>[10,11,15,18–22]</sup> on AM process optimization for steel has focused on samples with specific parameters, which cannot help determine an optimum processing window for preparing defect-free carbon steels. In addition, the optimization of the EB-PBF processing parameters is typically based on a trial-and-error method and extensive experimentation, which is time-consuming and expensive. A simple and effective prediction of the processing window to prepare defect-free carbon steel is a key challenge. In recent years, machine learning techniques have been increasingly used in the fields of AM and material development.<sup>[23–25]</sup> Aoyagi *et al.*<sup>[26]</sup> proposed a novel and efficient method for process parameter optimization based on support vector machine (SVM) to obtain internal-defect-free EB-PBF-processed Co–Cr alloys by optimizing 2D process parameters (current and scan speed). Gui *et al.*<sup>[27]</sup> verified the effectiveness of this method in optimizing the 3D parameters of carbon steels, making it possible for machine-learning techniques to predict the parameters under which EB-PBF-processed carbon steels can be prepared free of internal defects, thus producing carbon steels with an excellent combination of strength and ductility.

In this study, we used a new SVM approach for EB-PBF process optimization to predict and validate the printing window for S25C carbon steel without internal defects to obtain an excellent combination of mechanical properties. Three key EB-PBF process parameters, namely the current, scan speed, and line offset, were selected as inputs to the SVM to establish a suitable processing window corresponding to the 3D-printing parameters in the preparation of internal-defect-free S25C carbon steel. The use of several optimized EB-PBF parameters in the printing window to prepare defect-free samples resulted in unprecedented mechanical properties. After excluding the interference of internal defects, the relationship between the microstructure and mechanical properties and the deformation mechanism of the EB-PBF-S25C carbon steel could be revealed. Finally, we investigated the strengthening mechanism of S25C carbon steel after heat treatment.

## II. EXPERIMENTAL MATERIALS AND METHODS

### A. Virgin Powder and EB-PBF Process

The original powder selected in this study was S25C carbon steel powder prepared using the plasma-rotating electrode process (PREP) method. Table I shows its chemical composition. An EB-PBF machine (developed by The Technology Research Association for Future Additive Manufacturing (TRAFAM)) was used to print the samples. The printing process included four steps: raking a layer of powder, preheating, selective melting, and stage down. S25C carbon steel samples with a length of 12 mm, width of 12 mm, and height of 14 mm were printed on a SUS304 substrate, and the height of the support structure at the bottom of the sample was 3 mm. The accelerating voltage of the machine was set to 60 kV, and the preheating temperature of the substrate was set to 885 °C (1158 K) to avoid powder smoke. The XY scanning strategy was chosen for the printing process, in which the bidirectional scanning direction was rotated by 90 deg for each 75 μm layer.

### B. Material Characterization and Mechanical Property Tests

The particle size distribution of the virgin powder was measured using a laser particle size analyzer (LS230, Beckman Coulter), and the internal defects of the powder and S25C carbon steel were determined using X-ray CT (Comscantecno Co., Ltd., Yokohama, Japan). Three-dimensional rendering of the X-ray CT data and porosity analysis were performed using ExFact® VR software (Nihon Visual Science, Inc., Tokyo, Japan). The surface morphologies, cross-sectional microstructures of the powders, and microstructures of the S25C carbon steel were analyzed using a field-emission scanning electron microscope (FE-SEM, JEOL JSM-IT800) equipped with an electron backscatter diffraction detector (TSL-OIM, EDAX). Transmission electron microscopy (TEM; JEM-2100, JEOL, Tokyo, Japan) was used to reveal the microstructure of the carbon steel. The surface topography of S25C carbon steel was measured using the Keyence® VR-3200 wide-area 3D measurement system with *Sdr* (developed interface area ratio) as the surface roughness index, which can be expressed as follows:

$$Sdr = \frac{1}{A} \left[ \iint_A \left( \sqrt{1 + \left( \frac{\partial z(x,y)}{\partial x} \right)^2 + \left( \frac{\partial z(x,y)}{\partial y} \right)^2} - 1 \right) dx dy \right] \quad [1]$$

Here,  $A$  and  $|Z_{(x,y)}|$  are the target area and absolute value between the height of the mean plane and the height of the convex part or the depth of the concave part, respectively. The post heat treatment process was conducted in a vacuum furnace. The sequence was as follows: quenching (at 900 °C for 10 minutes), water-cooling, tempering (at 600 °C for 60 minutes), and water-cooling. At a strain rate of  $1.0 \times 10^{-3} \text{ s}^{-1}$ ,

**Table I. Chemical Composition of the S25C Carbon Steel Powder**

Element	C	Si	Mn	P	S	Fe
Composition (Wt Pct)	0.243	0.165	0.396	< 0.005	0.0131	bal.

the tensile properties of the as-built and heat-treated parts were measured using an INSTRON tensile machine at room temperature.

### C. Support Vector Machine (SVM) Algorithm for Predicting Internal Defects in EB-PBF-Processed Carbon Steels

The processing map constructed by SVM was used to predict the printing parameters of the EB-PBF-processed carbon steel without internal defects. Among the classification algorithms related to machine learning, SVM is ideal for solving binary classification problems. Its basic idea is to perform classification by mapping the input vector to a high-dimensional printing parameters space using a kernel function and building a hyperplane based on its classification labels to maximize the boundary distance between two classes.<sup>[28,29]</sup> That is, in the sample space, according to the training set  $D = \{(x_1, y_1), (x_2, y_2), (x_3, y_3)\}, y_i \in \{0, +1\}$ , an optimized hyperplane is selected to separate the data point to maximize the margin between the two classes. Here, the training set  $D$  was obtained from a dataset containing 16 experimental data points related to S30C carbon steels with an actual composition of mainly Fe-0.3C, which has been previously studied.<sup>[27]</sup> Although slight variations in the carbon composition may affect the microstructure, it has little effect on the melting and solidification behavior of carbon steels; therefore, this composition was used to predict the macroscopic defects in carbon steels in this study. The independent variables  $x_1, x_2$ , and  $x_3$  represent the printing parameters of the EB-PBF process, namely the current, speed, and line offset, respectively.  $x$  represents the printing parameter and  $y$  represents the internal defect state of the sample, with a value of 0 implying that the sample has internal defects and a value of 1 implying no internal defects. The decision function is as follows<sup>[26,30]</sup>:

$$f(x) = w^T x + b \quad [2]$$

where  $w$  and  $b$  are the vectors and scalars, respectively, which are variables. The following RBF kernel function was used in the SVM model<sup>[29-31]</sup>:

$$K(x, y) = e^{-\gamma \|x - y\|^2} \quad [3]$$

Here,  $x$  and  $y$  represent the printing parameter and internal defect state of the sample, respectively. The hyperparameters ( $\gamma$ ) and cost parameter ( $C$ ) were optimized through a combination of the grid search method and  $K$ -folder cross-validation to improve the performance of the model.  $K$ -folder cross-validation involves dividing the samples into  $K$  subsets; selecting

one subset at a time as the test set and the rest as the training set; the average number of misclassified samples tested is taken as the confirmation error for this cross-validation:

$$\sum_{i=1}^k \frac{l_i}{k} \quad [4]$$

where  $l_k$  is the number of misclassified samples during testing, and  $k$  is the repeat count.

## III. RESULTS

### A. Starting Powder Characteristics of S25C Carbon Steel

Figure 1(a) shows the surface morphology of the S25C powder, which is a PREP powder with a very high sphericity. Figures 1(b) and (c) show the SEM and EBSD images of the powder cross sections, respectively, where no pores can be found, and a clear martensitic structure can be observed in the individual particles. Figure 1(d) shows that the particle size of the S25C powder varies from 30 to 300  $\mu\text{m}$ , with an average size of 87.8  $\mu\text{m}$ . The overall characteristics of the powder in three dimensions were reconstructed using X-ray CT, allowing for a more accurate and comprehensive description of the internal morphology of the powder; Figure 1(e) shows the results. The pores are labeled by different colors according to their size; the pores in this powder are spherical and no larger than 50  $\mu\text{m}$ , with a porosity of only 0.0011 pct. The pores in the virgin powder remained in the parts constructed using EB-PBF, which affected their mechanical properties.<sup>[32]</sup> In summary, the S25C alloy powder with high sphericity and extremely low porosity is suitable for printing S25C carbon steel without internal defects.

### B. Optimized EB-PBF Processing Window for S25C Carbon Steels Predicted by SVM

Process maps and probability prediction internal defects of the S25C carbon steel were constructed using the SVM method, the details of which are reported in literature.<sup>[26,27]</sup> The optimized cost parameters ( $C = 0.6$ ) and hyperparameters ( $\gamma = 1.5$ ) obtained by the grid search method and  $K$ -folder cross-validation optimization was used as the modeling parameters for the SVM model. Figure 2 shows the constructed process maps. The top of each process map in Figure 2 shows the range of the corresponding line offset, where the horizontal and vertical axes represent the beam current and scan speed, respectively. The colors in the process maps indicate two possible areas, namely red and blue

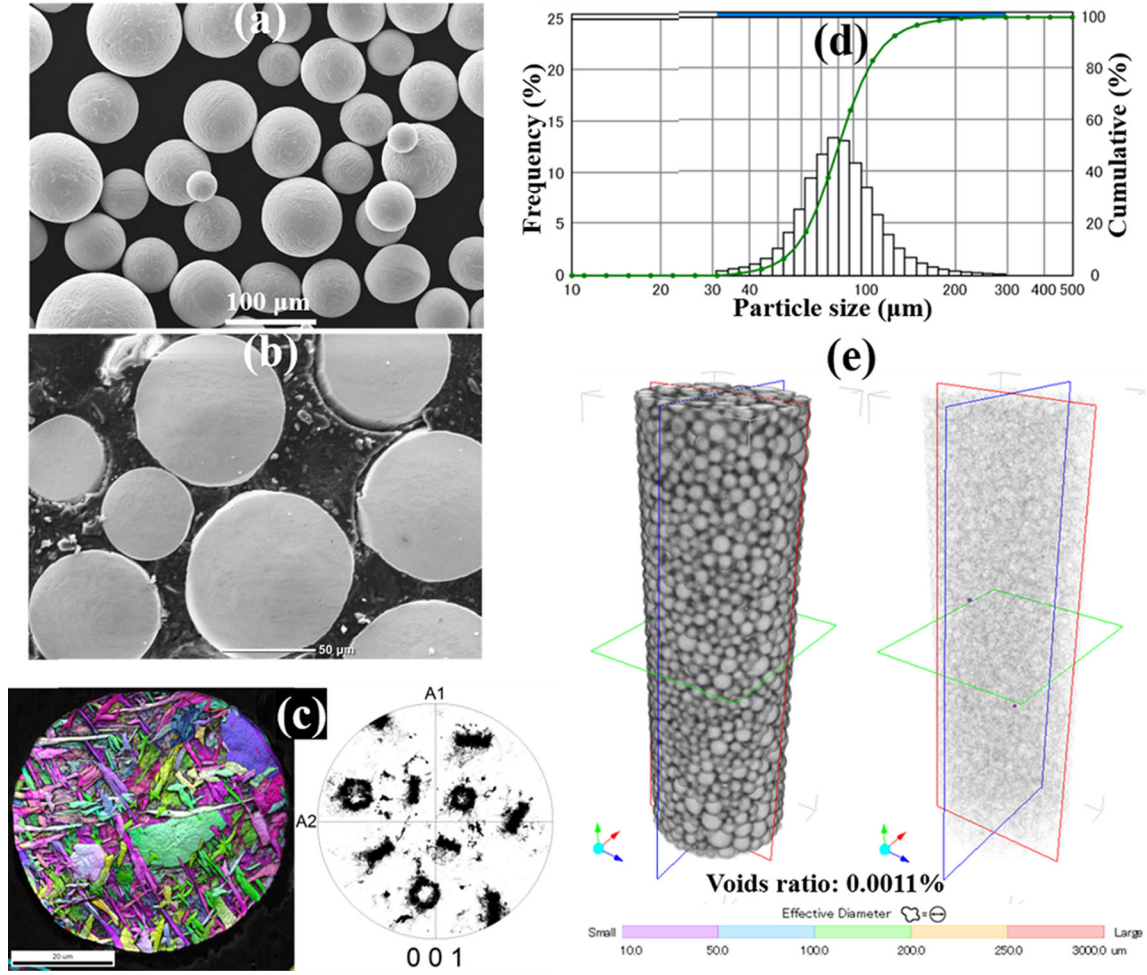


Fig. 1—Characteristics of the PREP-S25C powder: (a) SEM image of the surface morphology of the powder, (b) SEM image of the cross-section of the powder, (c) IPF map and pole figure of the cross-section of the powder, (d) Particle size distribution of the powder, and (e) X-ray CT measurements of the powder, in which internal voids are colored depending on their size.

areas, representing the printing parameters for samples with and without internal defects, respectively.

Compared with conventional methods for optimizing specific printing parameters, SVM process maps predict a processing window with a wider range of 3D printing parameters, making it possible to discover more parameters for manufacturing carbon steels with defect-free and desirable mechanical properties. Four sets of printing parameters for S25C were randomly selected from the blue area on the SVM process map. The four sets of printing parameters correspond to three energy density levels (see Table II for details). The line energy and energy density can be expressed as follows<sup>[26]</sup>:

$$E_{\text{volume}} = \frac{P}{V_{\text{scan}}} \quad [5]$$

$$E_{\text{volume}} = \frac{P}{V_{\text{scan}} L_{\text{offset}} Z_{\text{layer}}} \quad [6]$$

where  $E_{\text{line}}$ ,  $E_{\text{volume}}$ ,  $P$ ,  $V_{\text{scan}}$ ,  $L_{\text{offset}}$ , and  $Z_{\text{layer}}$  are the global energy density, beam power, scan speed, line offset, and layer thickness, respectively. Two subgroups

of the samples were considered for studying the microstructure and mechanical properties, in later sections. With the first group (E59, E76, and E175A), we compared the effects of different energy densities on the S25C specimens, and the effects of different combinations of printing parameters at the same energy density were evaluated using the second group (E175A and E175B).

### C. Surface Morphology and Internal Defects of EB-PBF-S25C Carbon Steels

Generally, components processed using EB-PBF exhibit even, uneven, and porous surface morphologies. Such an even surface not only makes the printed shape of the component more stable but also often corresponds to good internal quality owing to the layer-by-layer stacking characteristics of the EB-PBF technology. In the EB-PBF process, suboptimal parameter settings can lead to parts printed with a poor surface quality. In this section, we investigate four groups of samples printed with the parameters listed in Table II, the surface morphologies of which are shown in Figure 3.

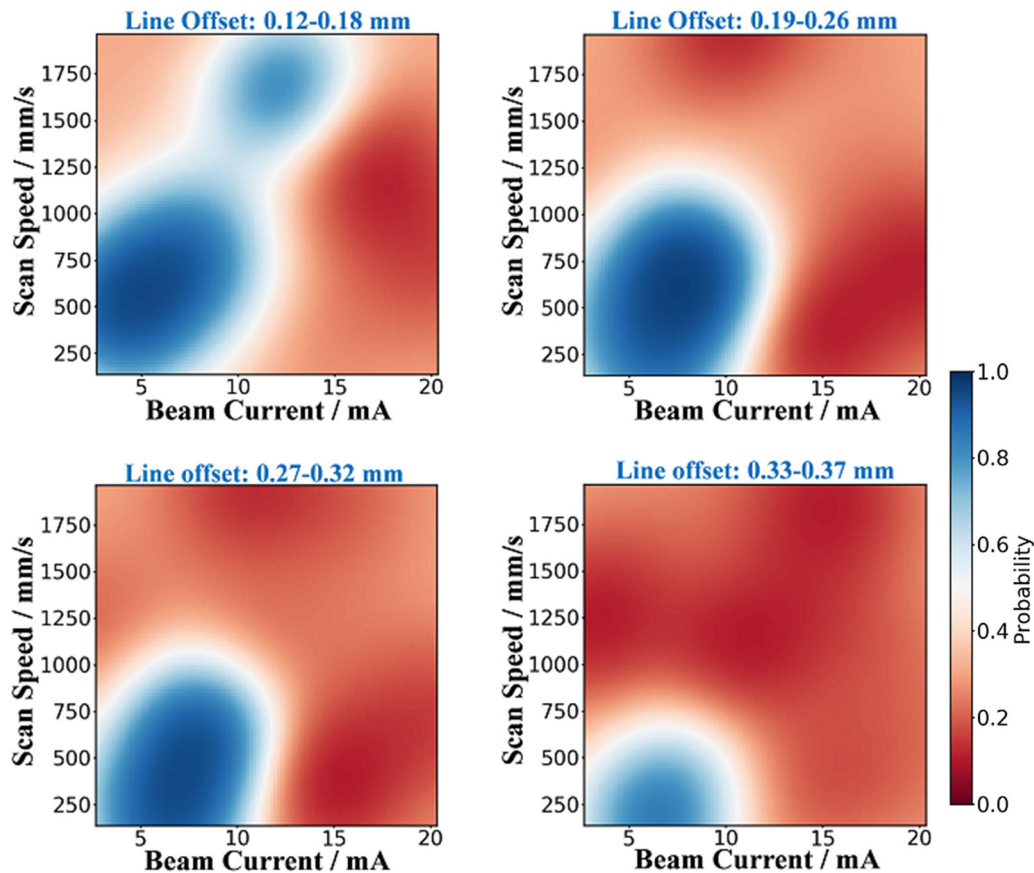


Fig. 2—Process maps of S25C constructed using the SVM as a function of the 3D printing parameters (beam current, scan speed, and line offset). Blue area (probability: 1.0) indicates that the surface morphology of the part printed using the processing parameters is predicted to be good (even surface) without internal defects, whereas the red area (probability: 0.0) indicates a poor (uneven or porous) surface with internal defects (Color figure online).

Table II. Four Sets of Printing Parameters Selected From the Blue Area Shown in Fig. 2

Name	Current (mA)	Scan Speed (mm s <sup>-1</sup> )	Line Offset (mm)	Energy Density (J mm <sup>-3</sup> )
E59	6.67	300	0.30	59
E76	9.37	317	0.31	76
E175A	9.63	260	0.17	175
E175B	8.00	300	0.12	175

Figure 3 shows four sets of optical images of the top surface of S25C, all with an even surface. To further quantify the surface quality,  $S_{dr}$  was used as an indicator of the surface roughness. The E59, E76, E175A, and E175B samples showed low  $S_{dr}$  values of 0.003, 0.004, 0.011, and 0.006, respectively, which also satisfy our previously derived quantitative criterion to obtain an even surface in EB-PBF-processed carbon steel ( $S_{dr} \leq 0.015$ ).<sup>[27]</sup>

Figure 4 shows the X-ray CT results of the central part of S25C parallel to the building direction. Clearly, none of the four sets of samples showed any evident internal defects. Only trace amounts of spherical pores could be observed, and both the size and shape were nearly identical to those of the virgin powder shown in Figure 1(e), which also indicates that no new defects

were introduced during the printing process. This validates the reliability and accuracy of the SVM process map shown in Figure 2.

#### D. Microstructures of the EB-PBF-S25C Carbon Steels

Figures 5(a) through (d) show the XRD patterns of S25C prepared with different printing parameters over a wide  $2\theta$  range (40 to 120 deg). Diffraction peaks corresponding to the (110), (200) and (211) crystal faces of the  $\alpha$ -Fe phase (bcc) can be clearly identified. Compared with the standard  $2\theta$  position of the Fe phase (JCPDS No. 06-0696), the  $2\theta$  positions of S25C slightly shifted to the left, implying the presence of lattice distortion. With the increase in the energy density, the diffraction peak of the Fe phase broadened,

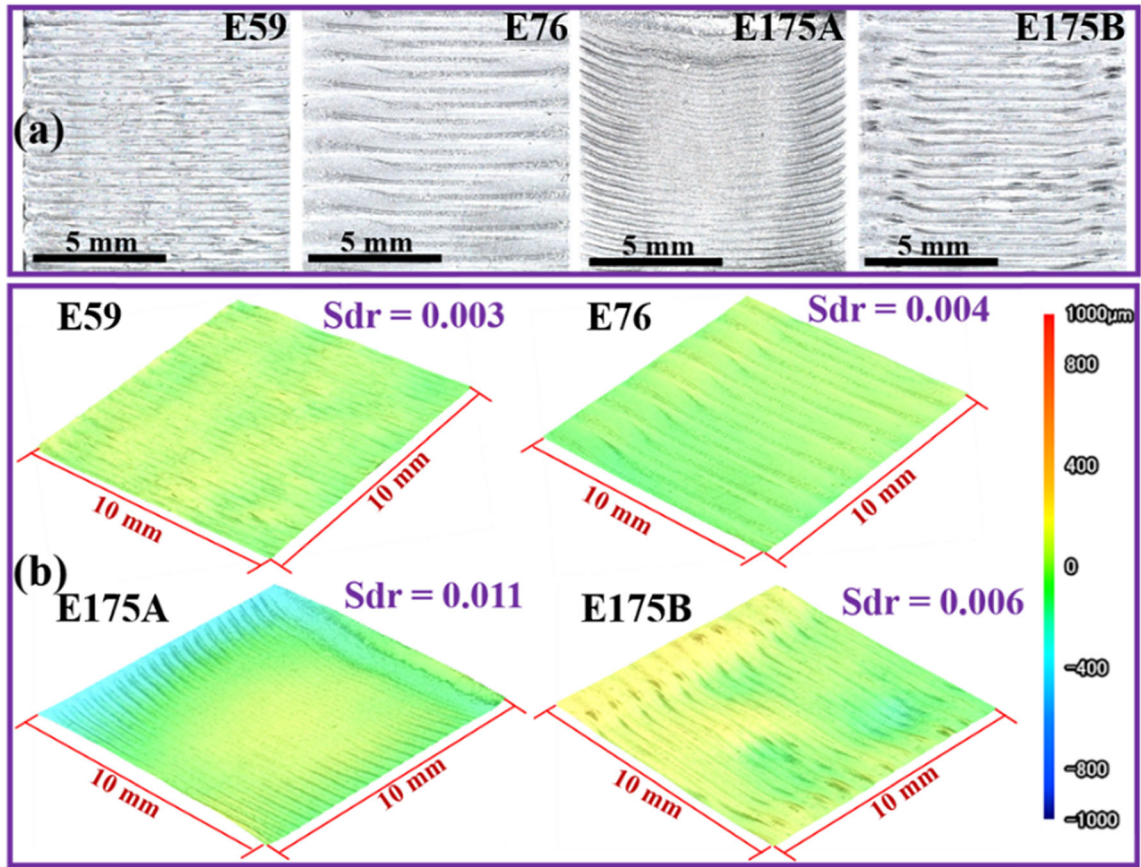


Fig. 3—(a) Digital images of the surface morphology of S25C with different printing parameters, (b) Three-dimensional surface topographical images and surface roughness (*Sdr*) values of S25C with different printing parameters.

indicating a higher degree of lattice distortion. Figure 6 shows the SEM morphologies of the four sets of samples along the printing direction, all of which contain both ferrite and pearlite. Further zooming in on the ferrite region, as shown in Figures 6(e) through (h), we can find a large amount of cellular structure.

To further understand the microstructures of the alloys at different energy densities and printing parameters, Figure 7 shows the detailed microstructural characteristics of the four alloys obtained using EBSD mapping, where the central area of the part along the cross-section of the building direction is shown. The inverse pole figure (IPF) maps show a gradual increase in the grain size with increasing energy density, which is not significantly affected by the consistent energy density or different combinations of printing parameters. Figure 7(e) shows the quantitative grain size results of the four alloys for samples E59, E76, E175A, and E175B: 51.2, 53.4, 79.8, and 80.9  $\mu\text{m}$ , respectively. The E59 and E76 samples at low and medium energy densities (Figures 7(a) and (b)) showed typical equiaxed crystals, whereas the E175A and E175B samples at high energy densities (Figures 7(c) and (d)) exhibited a side plate-like structure growing at an angle along the printing direction.

Figure 8 shows the corresponding IQ + GB boundary map for the map shown in Figure 7, where the green and blue lines represent the low-angle grain boundaries

(LAGBs, 2 to 15 deg) and high-angle boundaries (> 15 deg), respectively. The different samples showed different numbers of LAGBs. Figure 8(e) shows the misorientation angles of the E59, E76, E175A, and E175B samples, with  $\theta_{\text{avg}}$  showing a decreasing trend at 28.2, 26.6, 24.2, and 23.9 deg, respectively, with the increase in the energy density. Kernel average misorientation (KAM) calculations are often used to measure the density of dislocations and the residual stresses within grains.<sup>[33]</sup> For the KAM calculation at point (*P*<sub>*i*</sub>), the misorientation between the central point (kernel) and the surrounding points (each labeled as *j*) is calculated and then averaged using the following expression<sup>[34]</sup>:

$$\text{KAM}_{P_i} = \frac{1}{N} \sum_{j=1}^N \Delta\theta_{ij}, \Delta\theta_{ij} < 5^\circ. \quad [7]$$

Here, *N* is the number of surrounding points, and  $\Delta\theta_{ij}$  is the corresponding mismatch between *i* and *j*. Higher KAM values represent a higher dislocation density in the grains, based on which the KAM profiles and quantitative analyses of the four samples are shown in Figure 9. A comparison of the results in Figures 9 and 8 shows that the high-value positions in the KAM profiles are directly correlated with LAGBs. The quantitative KAM results in Figures 9(e) through (h) show a

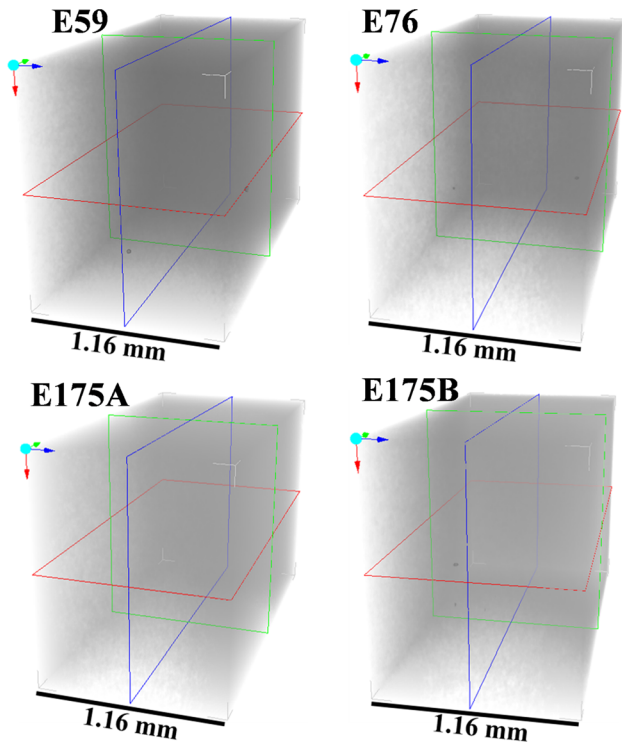


Fig. 4—X-ray CT measurements of S25C prepared with different printing parameters.

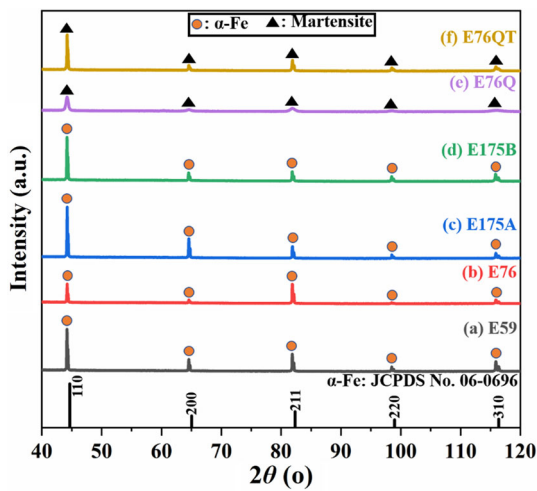


Fig. 5—XRD results of S25C carbon steel prepared with different printing parameters and after heat treatment.

significant increase in the KAM values with increasing sample energy density, with mean values of 0.40, 0.42, 0.45, and 0.50, respectively, that is, a gradual increase in the dislocation density.

#### E. Microstructures of the EB-PBF-S25C Carbon Steels After Heat Treatment

Figure 10 shows the microstructure of the E76 sample after quenching and tempering, where the equiaxed crystals are completely transformed into a very fine slate-like structure compared with the as-built sample.

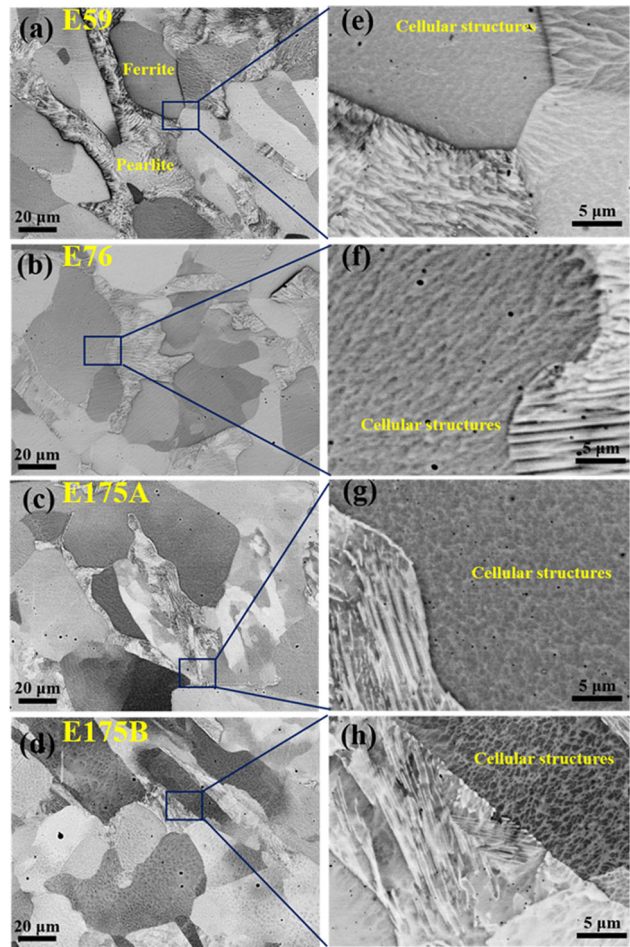


Fig. 6—(a) to (d) SEM images of S25C prepared with different printing parameters, (e) to (h) Enlarged views corresponding to (a)–(d).

The quenched samples were named E76Q, and the quenched and tempered samples were called E76QT. The (001) pole plot (Figure 10(a)) for E76Q shows a typical Kurdjumov–Sachs orientation relationship:

$$(111)_{\gamma} // (011)_{\alpha'} [\bar{1}01]_{\gamma} // [\bar{1}\bar{1}1]_{\alpha'} \quad [8]$$

Therefore, the E76Q samples exhibited a typical lath martensitic structure. This result is supported by the XRD peaks of these samples shown in Figure 5(e), where the diffraction peaks are at the same positions as those of the  $\alpha$ -Fe phase (bcc) owing to the similarity in the ferrite and martensitic crystal structures. Nevertheless, the XRD peaks were broader than those of the as-built sample, indicating that the heat treatment procedure introduced a lattice strain, with the E76Q sample having the broadest peak, which suggests the highest lattice strain. The KAM plot for the E76Q sample (Figures 10(b) and (c)) shows a very high KAM (1.40), implying a high dislocation density. In contrast, the KAM plot for the E76QT sample (Figures 10(e) and (f)) shows a significantly lower value (1.01), indicating a significant decrease in the dislocation density because of the restoration that occurred during the tempering

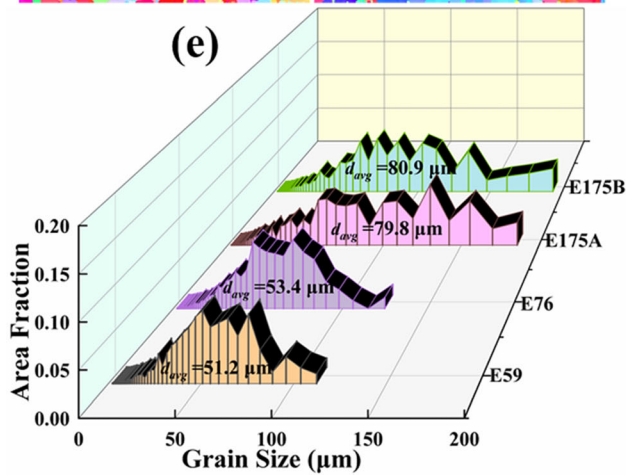
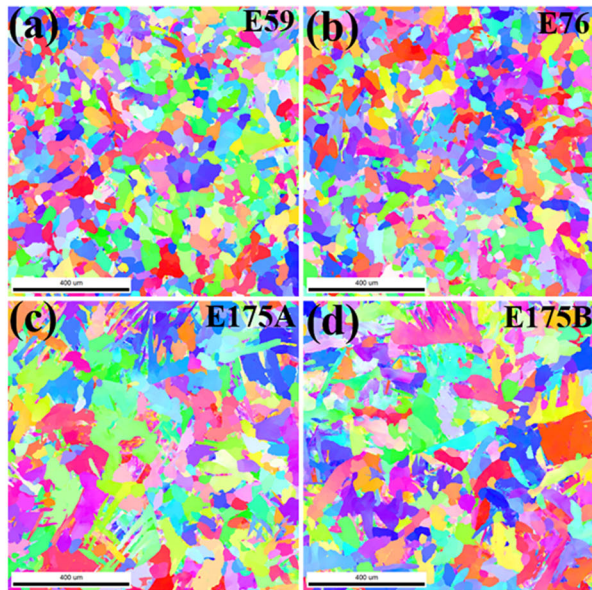


Fig. 7—(a) to (d) Inverse pole figure (IPF) maps and (e) Grain size of S25C prepared with different printing parameters.

process; however, both the values were significantly higher than those of the as-built sample.

#### F. Mechanical Properties of EB-PBF-S25C Carbon Steels and After Heat Treatment

Tensile tests were performed at room temperature along the building directions of the alloys prepared using different printing parameters. Figure 11(a) shows the tensile curves of the specimens. The ultimate tensile strength (UTS) and yield strength (YS) varied slightly with increasing energy density, and the elongation increased and then decreased, with the sample E76 having the highest UTS (459.3 MPa) and elongation (57.6 pct). For the same energy density (E175A and E175B), the differences in the elongation and strength were lower. This shows that for the EB-PBF-S25C

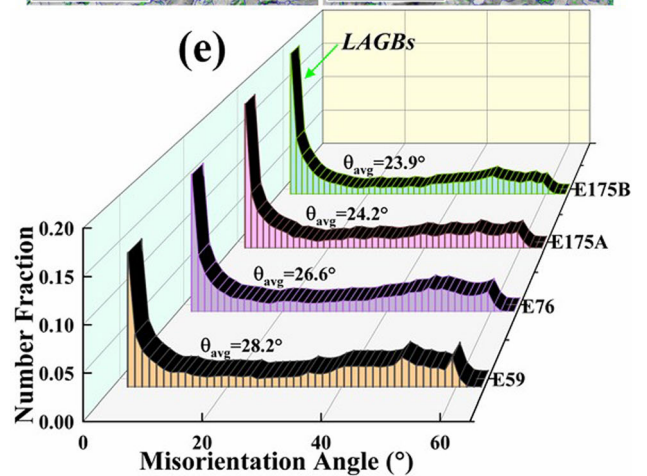
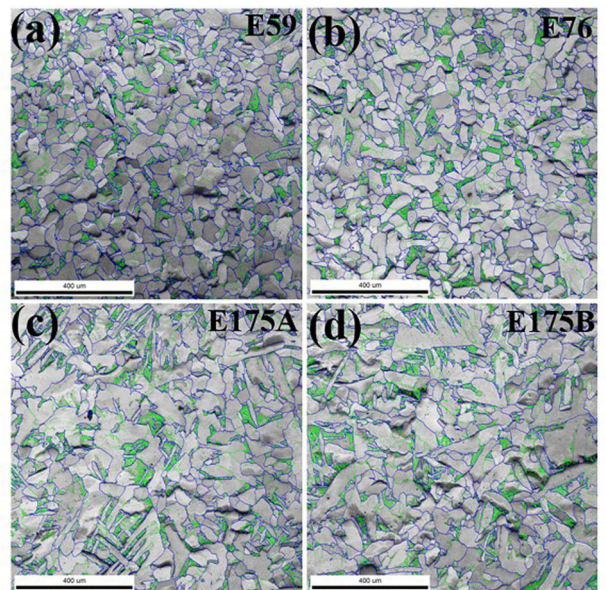


Fig. 8—(a) to (d) IQ + GB maps and (e) Misorientation angle of S25C prepared with different printing parameters.

carbon steel without internal defects, the mechanical properties were mainly controlled by the energy density and that changing the combination of the printing parameters had a limited effect under the same energy density. After the quenching treatment of the E76Q sample, the UTS increased to approximately 1722.5 MPa, while the elongation decreased to 16.8 pct, and after further tempering, the UTS and elongation of the E76QT sample were 722.7 MPa and 44.2 pct, respectively. Figure 11(b) shows a comparison between the mechanical properties of the S25C carbon steel used in this study and other S25C carbon steels manufactured *via* conventional processing.<sup>[35,36]</sup> The S25C carbon steel in this work exhibited superior elongation, and after quenching, an ultrahigh strength, both of which were significantly higher than S25C carbon steels manufactured *via* conventional processing reported in literature.<sup>[35,36]</sup>



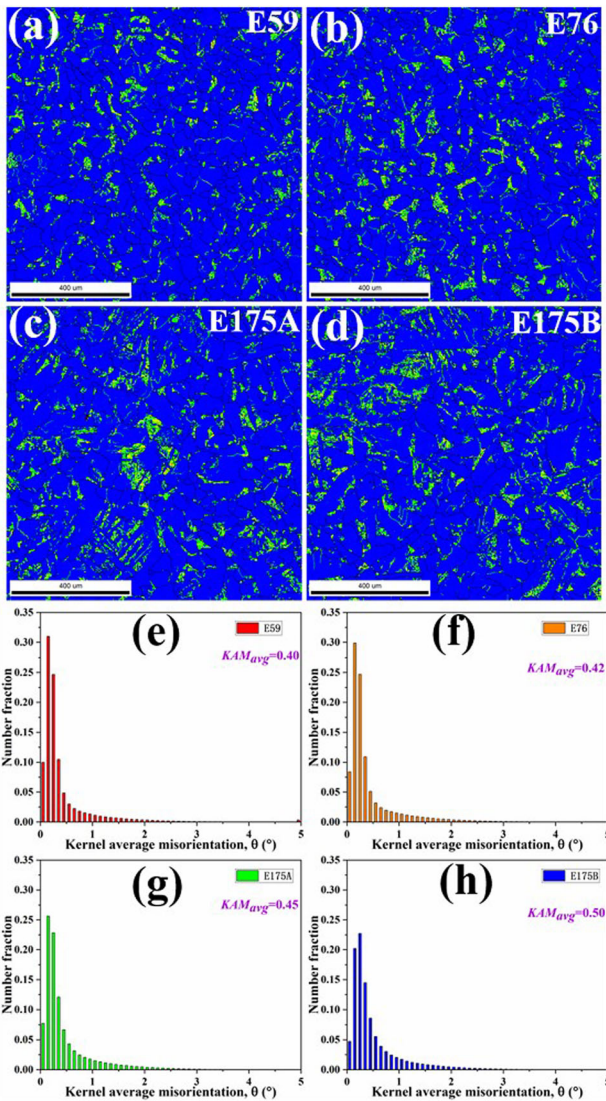


Fig. 9—(a) to (d) KAM maps and (e) to (h) KAM values of S25C prepared with different printing parameters.

## IV. DISCUSSION

### A. Proposed SVM Model Optimization Method vs Conventional Methods Employed for the EB-PBF-S25C Carbon Steels

It is essential to establish an optimized processing window to prepare a S25C sample without internal defects. In this study, by means of SVM model optimization using only 16 experimental data points obtained from literature<sup>[27]</sup> as inputs, we identified a new and broad S25C processing window. The validity of the model was verified experimentally by printing with four randomly selected sets of printing parameters from the processing window and achieving record-high strength and ductility in S25C carbon steel.

Conventional optimization methods are restrictive, as they can only optimize specific parameters, whereas the EB-PBF process has a high-dimensional and complex parameter space, where different combinations of the printing parameters yield specimens with different

properties and microstructures. As representative examples, 3D processing parameters, namely the beam current, scan speed, and line offset, were considered in this study, with ranges of 2–20 mA, 200–2000 mm/s, and 0.12–0.37 mm, respectively. In the case of optimization using conventional orthogonal experimentation and trial-and-error method, assuming that the beam current is taken at intervals of 2 mA, the scan speed at intervals of 100 mm/s, and the line offset at intervals of 0.05 mm, the total number of parameter combinations would be  $9 \times 18 \times 5 = 810$ . Conventional optimization methods cannot be applied individually, making it difficult to find processing windows for high-performance materials.

Although the focus of this study was on S25C carbon steel, the new SVM model optimization method can be extended to the EB-PBF process optimization and mechanical property design of other alloys.

### B. Deformation Mechanisms of EB-PBF-S25C Carbon Steels

As shown in Figure 11, the S25C carbon steels used in this study exhibit good strength and unprecedented plasticity. To investigate the mechanical properties, the microstructure of S25C was examined. Figure 12 shows a TEM image of the morphology of the E76 sample. Figure 12(a) shows the grain boundaries separating the ferrite and pearlite. The pearlite region has two main morphologies. Figure 12(b) shows the first morphology with irregular cementite particles accompanied by numerous dislocations, which help effectively strengthen the alloy. The pearlite region shown in Figure 12(d) is the second type, which has parallel and straight cementite particles without dislocations, which is conducive to the plasticity while enhancing strength. In contrast, as shown in the bright-field phase and diffraction spots in Figures 12(e) through (h), sub-grains, very small amounts of dislocations, and nanoparticles with a size of approximately 10 nm can be observed in ferrite, which is beneficial for plasticity.

To clarify the deformation mechanism of the S25C carbon steels with excellent plasticity, we obtained the EBSD maps of the E76 sample at different tensile strains and fracture morphologies, as shown in Figure 13. Figures 13(a) through (d) show the IPF + IQ and KAM + IQ plots for deformation strains of 0, 10, 30, and 57.6 pct (fracture), respectively. Figure 13(a) shows that the alloy with 0 pct deformation exhibits equiaxed crystals and a small number of dislocations, which are mainly in the pearlite region. At 10 pct deformation, equiaxed crystals were still predominant, and the number of dislocations increased significantly. When further increasing the deformation to 30 pct, the grains gradually elongated in the tensile direction, and dislocations were clustered in almost all the grains. When the deformation was 57.6 pct (fracture), the grains were substantially elongated, and severe deformation occurred. As shown in the KAM diagram, all the grains are clustered with dislocations and the KAM values are very high, implying the presence of a large number of dislocations. Cracks can also be observed in

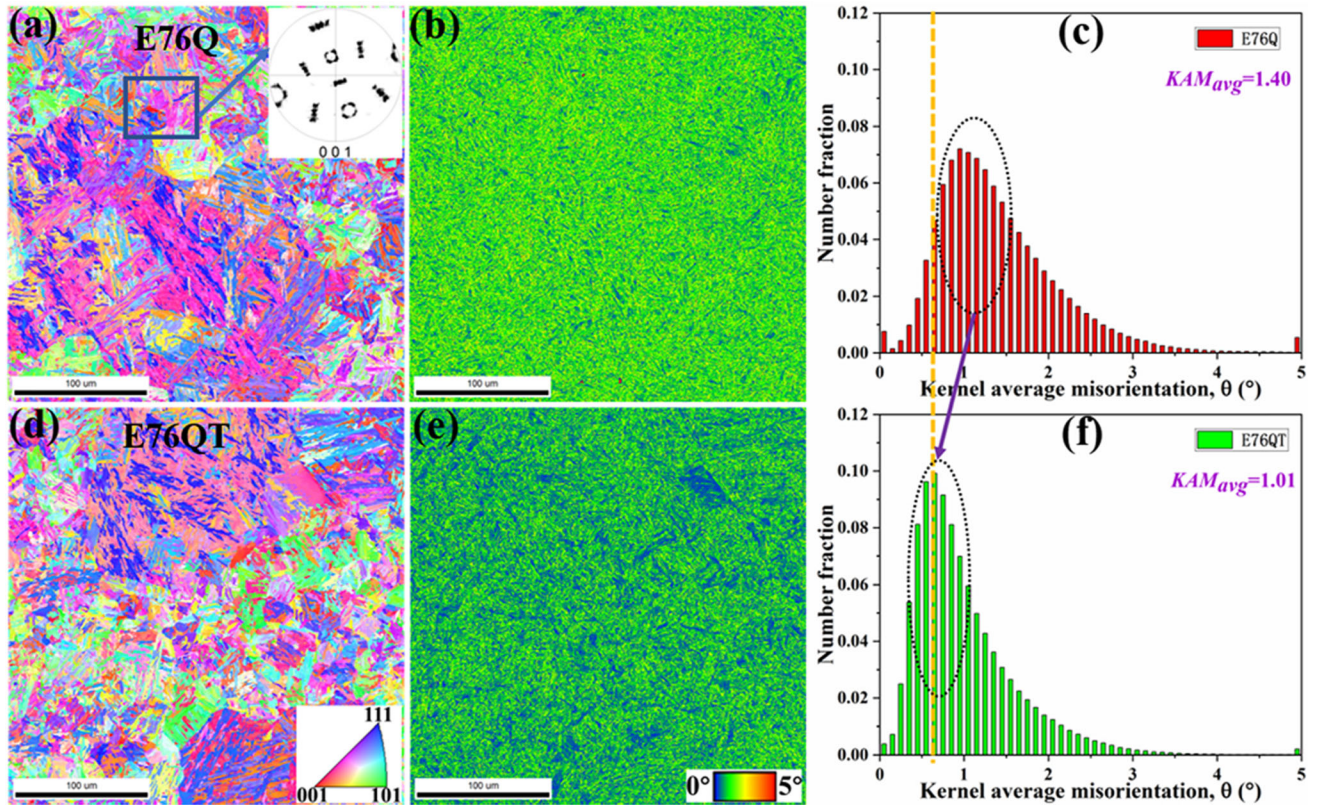


Fig. 10—(a, d) IPF maps, (b, e) KAM maps, and (c, f) KAM values of E76Q and E76QT samples, respectively.

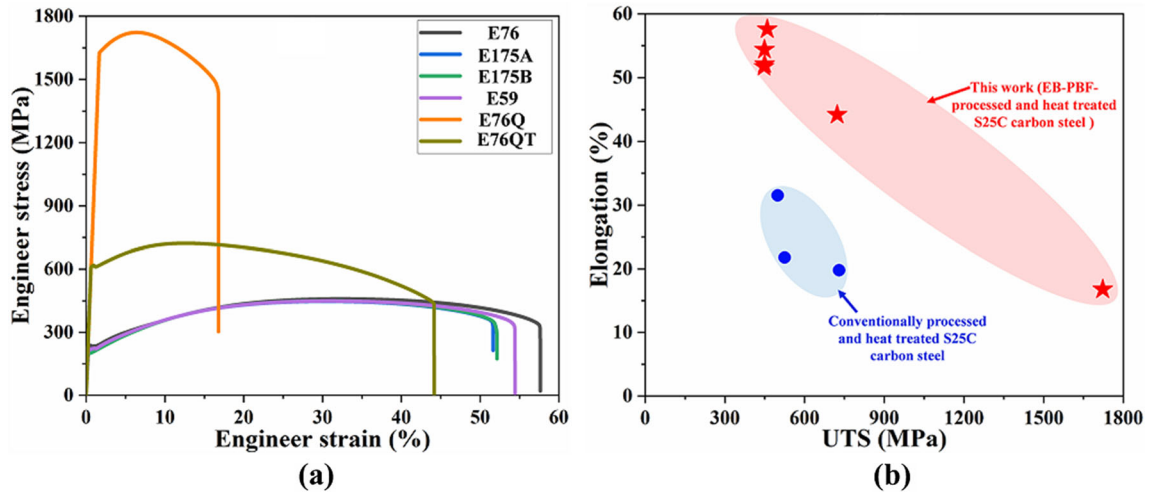


Fig. 11—Mechanical properties of S25C carbon steels: (a) Engineering stress–strain tensile curves of S25C carbon steels under different conditions at room temperature, (b) Comparison of UTS and elongation with S25C carbon steels manufactured *via* conventional processing in literature.<sup>[35,36]</sup>

Figure 13(d), and an enlarged view of the fractured sample is shown in Figure 13(e), where cracks appear mainly at the pearlite junction. Figure 13(f) presents the fracture morphology of the E76 sample, containing a brittle fracture characteristic of a cleavage fracture and a ductile fracture characteristic of dimples, which are formed by the heterogeneous microstructure comprising brittle pearlite and ductile ferrite. The dimple size also

varied, and the very small dimples confirmed the presence of a cellular structure in the ferrite. A comparison between the IPF plots for different deformation amounts revealed a change in the grain color, which is due to the fact that the grain color represents the grain orientation and that the deformation mode is mainly based on slip deformation.

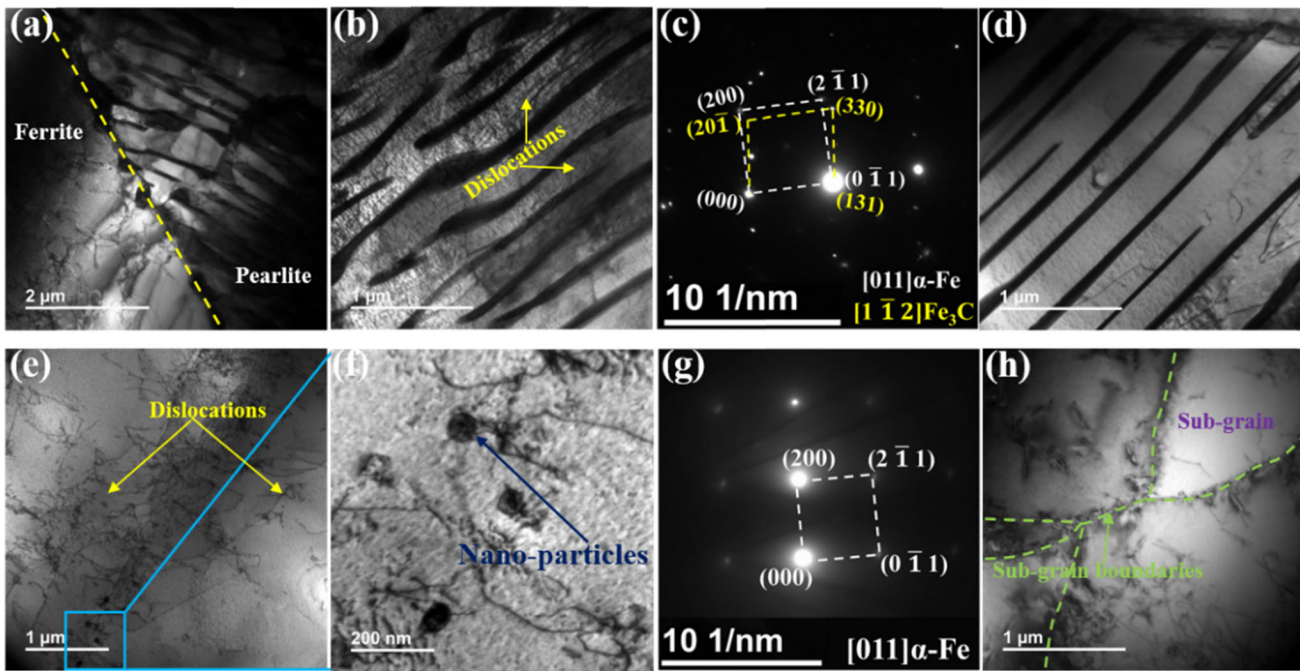


Fig. 12—TEM morphologies of the E76 sample: (a) Grain boundaries separating ferrite and pearlite, (b) Pearlite region with irregular cementite particles accompanied by numerous dislocations, (c) SAED pattern of the pearlite region, (d) Pearlite region with parallel and straight cementite particles without dislocations, (e) Very small amounts of dislocations in the ferrite, (f) Nanoparticles in the ferrite, (g) SAED pattern of the ferrite region, and (h) Sub-grains in the ferrite.

To further clarify the deformation mechanism of the S25C carbon steel, the E76 sample before fracture (deformation strain at 50 pct) was observed. Figure 14(a) shows cracks appearing in pearlite, whereas no cracks can be observed in the surrounding ferrite. An enlarged view of the crack location (Figure 14(b)) shows that the cracks appeared in the irregular pearlite region indicated in yellow, whereas there was no crack in the regular pearlite region indicated in red. This is because of the large number of dislocations and irregularly shaped cementite particles in the irregular pearlite region, which hindered the expansion of dislocations and slips and easily produced dislocation plugging, leading to the generation of cracks. Further, the EBSD plot corresponding to Figure 14(b) is further observed as shown in Figures 14(c) through (e). The lower KAM plot values at the crack locations are due to the release of energy and residual stress from the fracture as well as the transfer of dislocations into the adjacent ferrite, corresponding to the dislocation and grain orientation changes that were found to be significantly higher at the ferrite location than at other locations in the grain. The presence of this heterogeneous structure allows ferrite to effectively release the dislocations created in pearlite and help regulate plasticity. Figure 14(f) shows a schematic of the deformation mechanism. At the early stages of deformation, the dislocations in pearlite can be effectively transferred to the adjacent ferrite, and with the increase in deformation, the dislocations in the irregular pearlite area accumulate to a certain extent and cannot be transferred quickly, in which case an initial crack is formed. Therefore, controlling the proportions of ferrite and pearlite, as well as increasing the content of regular

pearlite, is a direction for future research to further improve the mechanical properties of EB-PBF-processed carbon steels.

### C. Strengthening Mechanisms of EB-PBF-S25C Carbon Steels After Heat Treatment

After quenching, the strength of the E76Q sample increased to an unprecedented level compared with that of the conventionally processed carbon steel. After further tempering, although the strength reduced, there was a substantial increase in plasticity, and the mechanical properties were overall not ideal. Hence, it is important to reveal the strengthening mechanism of heat-treated EB-PBF-processed carbon steels. First, the morphology of the quenched sample E76Q was observed by TEM. Figure 15 shows the bright-field phase, dark-field phase, and diffraction spots of lath martensite, around which a large number of dislocation entanglements can be observed. These numerous dislocations and the presence of martensite help effectively resist deformation and produce a work-hardening behavior, thereby substantially increasing the strength of carbon steel.

Figure 16 shows the TEM morphology of the E76QT sample after further tempering, where a dramatic change can be observed compared with the quenched microstructure, attributed to the restoration during tempering at 600 °C. Figures 16(a) through (c) show that the lath martensite is almost completely retained, while the sparse dislocation lines also indicate a significant reduction in the dislocation content of the carbon steel after tempering. Figures 16(d) through (f) show the

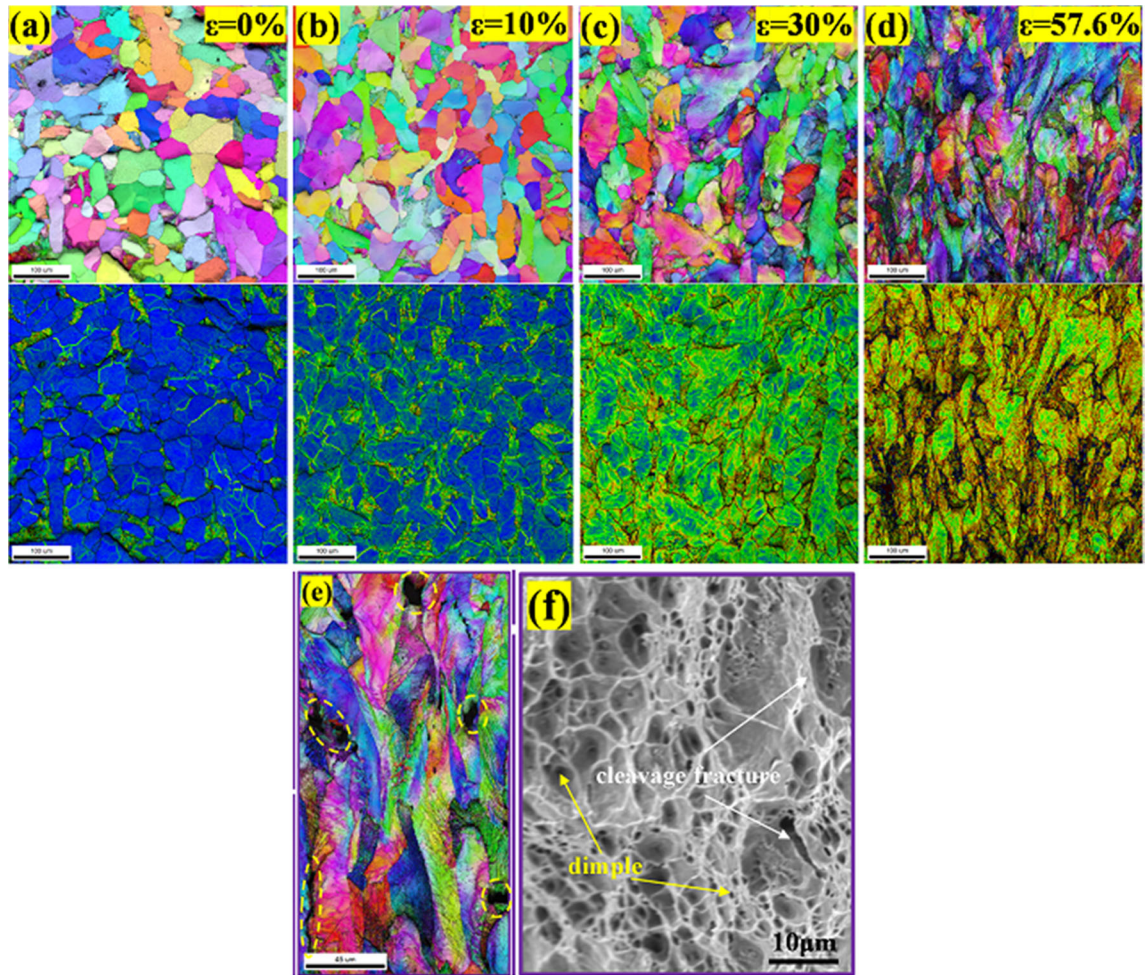


Fig. 13—IPF + IQ and KAM + IQ plots of the E76 sample with deformation strains of (a) 0 pct, (b) 10 pct, (c) 30 pct, and (d) 57.6 pct (fracture), (e) Enlarged view of the fractured sample E76, (f) Fracture morphology of the E76 sample.

presence of cementite particles in the lamellar martensite and ferrite matrix due to the formation of cementite as a result of the precipitation of supersaturated carbon in the Fe phase during the tempering process. The cementite, lath martensite, and dislocation lines resulted in an excellent combination of strength and plasticity in the E76QT sample.

## V. CONCLUSIONS

In this study, a novel SVM model optimization method was developed to identify a wide processing window in the manufacturing of EB-PBF-S25C carbon steel without internal defects. Samples with unprecedented mechanical properties could be successfully printed. The relationships between EB-PBF processing parameters, heat treatment, microstructure, and mechanical properties of various samples were investigated. The main conclusions are as follows:

- (1) Samples with a lower energy density showed a completely equiaxed crystal structure, whereas those with a higher energy density exhibited an

equiaxed crystal and side plate-like structure. The S25C parts mainly comprised ferrite, pearlite, and cellular structures. The pearlite region contained parallel and straight cementite particles without dislocations and irregular cementite particles with numerous dislocations.

- (2) With the increase in the energy density, the grain size and dislocation density increased, and the elongation initially increased and then decreased. Samples with the same energy density exhibited similar microstructures and mechanical properties. The E76 sample had an optimum strength and elongation combination of 459.3 MPa and 57.6 pct.
- (3) The pearlite region with irregular cementite particles was the first to crack during deformation; the cracks then gradually expanded into the surrounding area. Ferrite, cellular structures, and pearlite with parallel and straight cementite particles could effectively modulate the deformation by slip and enhance the plasticity of the S25C parts.
- (4) After quenching, the strength of the E76Q sample improved to an unprecedented value of

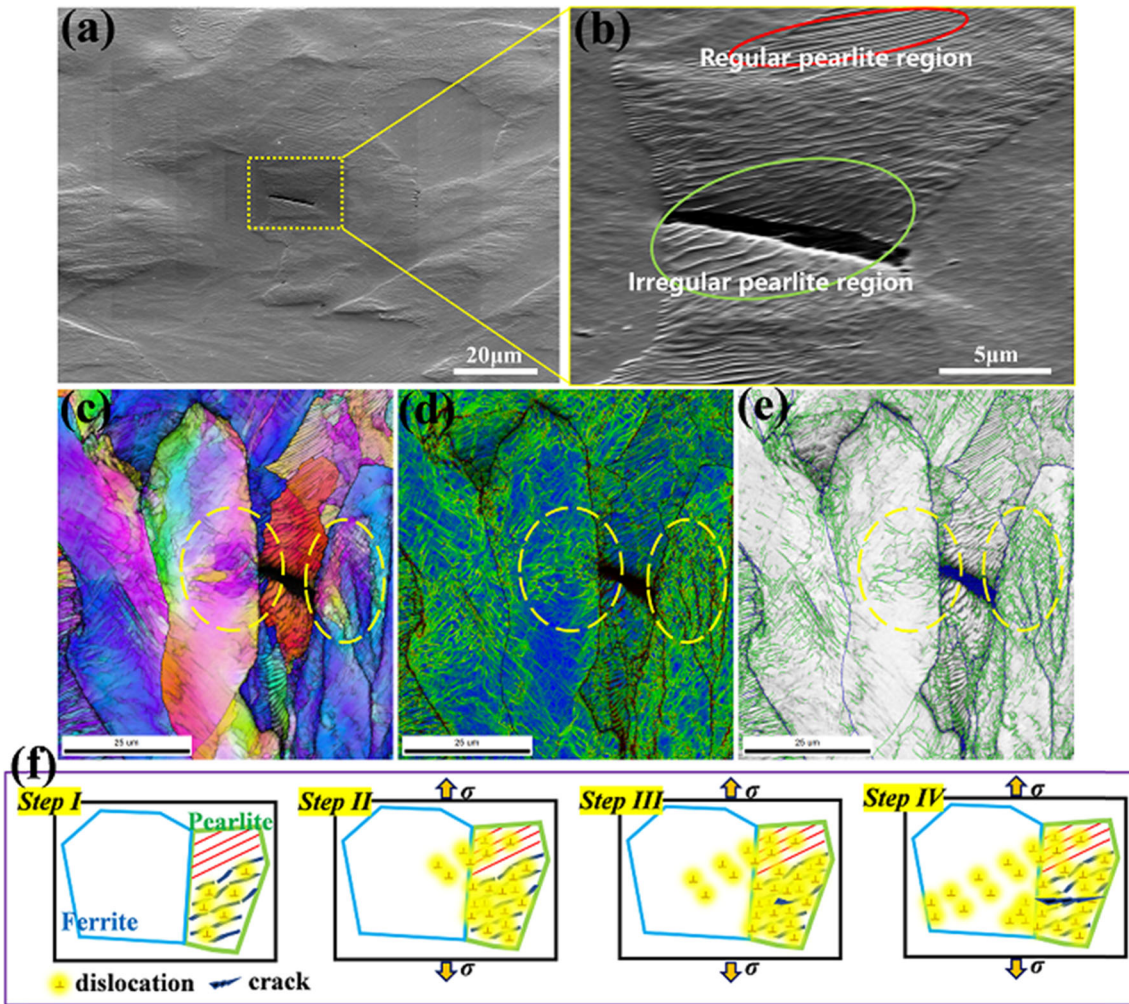


Fig. 14—(a) SEM image of S25C carbon steel with a deformation strain of 50 pct, (b) Enlarged view corresponding to (a); (c) IPF + IQ map, (d) KAM + IQ map and (e) GB + IQ map corresponding to (a); (f) Schematic of the deformation mechanism of S25C carbon steel.

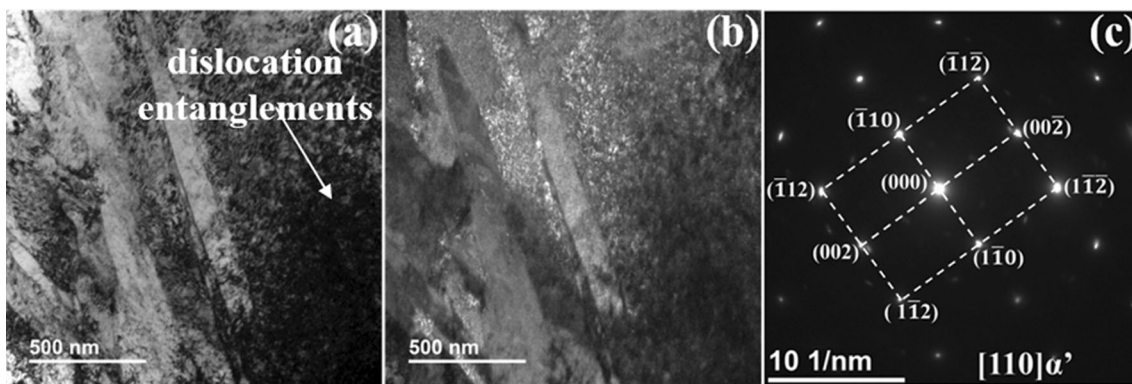


Fig. 15—TEM morphologies of the E76Q sample: (a) bright fields, (b) dark fields and (c) corresponding SAED pattern.

1722.5 MPa owing to the presence of martensite and dislocation entanglements, with an elongation of 16.8 pct. In comparison, the strength of the E76QT sample decreased after further

tempering, and the plasticity evidently increased, with an optimum strength and elongation combination of 722.7 MPa and 44.2 pct, respectively. The microstructure of the E76QT sample

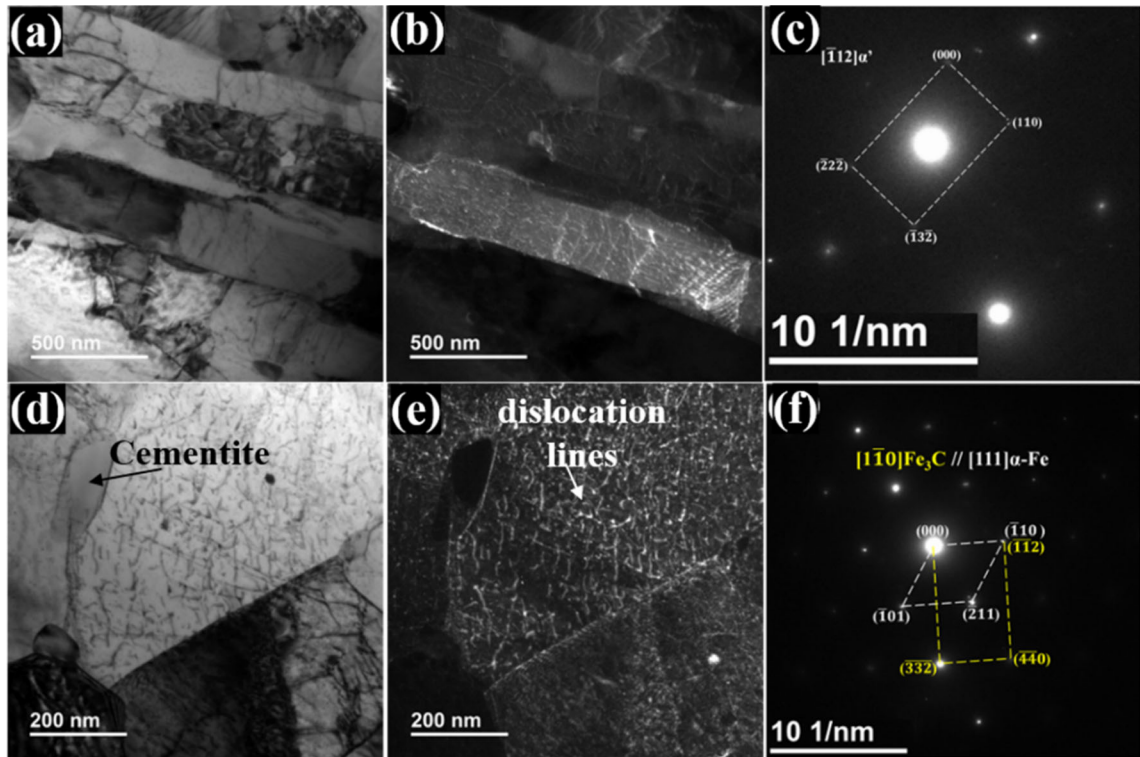


Fig. 16—TEM morphologies of the E76QT sample, (a) to (c) and (d) to (f) corresponding to bright fields, dark fields, and SAED pattern of lamellar martensite and cementite, respectively.

comprised lath martensite, cementite particles, and sparse dislocation lines.

#### ACKNOWLEDGMENTS

This study was based on the results of project JPNP19007, commissioned by the New Energy and Industrial Technology Development Organization (NEDO). This work was also supported by JSPS KAKENHI (Proposal No. 21K03801) and the Inter-University Cooperative Research Program (Proposal Nos. 18G0418, 19G0411, and 20G0418) of the Cooperative Research and Development Center for Advanced Materials, Institute for Materials Research, Tohoku University, Japan. It was also supported by the Council for Science, Technology, and Innovation (CSTI), Cross-ministerial Strategic Innovation Promotion Program (SIP), and “Materials Integration” for the Revolutionary Design System of Structural Materials (Funding Agency: JST). Yunwei Gui acknowledges the financial support provided by the China Scholarship Council (Grant No. 201908410208).

#### CONFLICT OF INTEREST

The authors declare that they have no competing financial interests or personal relationships that may have influenced the work reported in this study.

#### OPEN ACCESS

This article is licensed under a Creative Commons Attribution 4.0 International License, which permits use, sharing, adaptation, distribution and reproduction in any medium or format, as long as you give appropriate credit to the original author(s) and the source, provide a link to the Creative Commons licence, and indicate if changes were made. The images or other third party material in this article are included in the article’s Creative Commons licence, unless indicated otherwise in a credit line to the material. If material is not included in the article’s Creative Commons licence and your intended use is not permitted by statutory regulation or exceeds the permitted use, you will need to obtain permission directly from the copyright holder. To view a copy of this licence, visit <http://creativecommons.org/licenses/by/4.0/>.

#### REFERENCES

1. H.L. Wei, T. Mukherjee, W. Zhang, J.S. Zuback, G.L. Knapp, A. De, and T. DebRoy: *Prog. Mater. Sci.*, 2021, vol. 116, 100703.
2. H. Bikas, P. Stavropoulos, and G. Chryssolouris: *Int. J. Adv. Manuf. Technol.*, 2016, vol. 83, pp. 389–405.
3. T. DebRoy, H.L. Wei, J.S. Zuback, T. Mukherjee, J.W. Elmer, J.O. Milewski, A.M. Beese, A. Wilson-Heid, A. De, and W. Zhang: *Prog. Mater. Sci.*, 2018, vol. 92, pp. 112–224.
4. S. Pan, G. Yao, Y. Cui, F. Meng, C. Luo, T. Zheng, and G. Singh: *Tungsten*, 2022, vol. 5, pp. 1–31.
5. M. Galati and L. Iuliano: *Addit. Manuf.*, 2018, vol. 19, pp. 1–20.
6. C. Körner: *Int. Mater. Rev.*, 2016, vol. 61, pp. 361–77.

7. R.W. Vanderbeck and E.H. Phelps: *Ind. Eng. Chem.*, 1959, vol. 51, pp. 1178–84.
8. L. Zhang, Y. Jin, X. Wang, J. Cai, and Q. Guan: *High Temp. Mater. Process.*, 2019, vol. 38, pp. 444–51.
9. Y.H. Song, M. Tane, and H. Nakajima: *Mater. Sci. Eng. A*, 2012, vol. 534, pp. 504–13.
10. O. Andreau, I. Koutiri, P. Peyre, J.D. Penot, N. Saintier, E. Pessard, T. De Terris, C. Dupuy, and T. Baudin: *J. Mater. Process. Technol.*, 2019, vol. 264, pp. 21–31.
11. M. Garibaldi, I. Ashcroft, M. Simonelli, and R. Hague: *Acta Mater.*, 2016, vol. 110, pp. 207–16.
12. P. Bajaj, A. Hariharan, A. Kini, P. Kürnsteiner, D. Raabe, and E.A. Jägle: *Mater. Sci. Eng. A*, 2020, vol. 772, 138633.
13. H.D. Carlton, A. Haboub, G.F. Gallegos, D.Y. Parkinson, and A.A. MacDowell: *Mater. Sci. Eng. A*, 2016, vol. 651, pp. 406–14.
14. Y. Gui, H. Bian, K. Aoyagi, and A. Chiba: *Mater. Lett.*, 2022, vol. 328, 133096.
15. M. Akita, Y. Uematsu, T. Kakiuchi, M. Nakajima, and R. Kawaguchi: *Mater. Sci. Eng. A*, 2016, vol. 666, pp. 19–26.
16. S. Lee, J. Kim, D.S. Shim, S.H. Park, and Y.S. Choi: *Met. Mater. Int.*, 2020, vol. 26, pp. 708–18.
17. J.J. Lewandowski and M. Seifi: *Annu. Rev. Mater. Res.*, 2016, vol. 46, pp. 151–86.
18. D. Junker, O. Hentschel, M. Schmidt, and M. Merklein: *Key Eng. Mater.*, 2015, vol. 651–653, pp. 707–12.
19. T. Niendorf, S. Leuders, A. Riemer, H.A. Richard, T. Tröster, and D. Schwarze: *Metall. Mater. Trans. B*, 2013, vol. 44B, pp. 794–96.
20. E. Santecchia, P. Mengucci, A. Gatto, E. Bassoli, S. Defanti, and G. Barucca: *Materials*, 2019, vol. 12, p. 2342.
21. C. Wang, X. Tan, E. Liu, and S.B. Tor: *Mater. Des.*, 2018, vol. 147, pp. 157–66.
22. H. Chen, D. Gu, L. Deng, T. Lu, U. Kühn, and K. Kosiba: *J. Mater. Sci. Technol.*, 2021, vol. 89, pp. 242–52.
23. S. Nasiri and M.R. Khosravani: *J. Mater. Res. Technol.*, 2021, vol. 14, pp. 1137–53.
24. C. Wang, X.P. Tan, S.B. Tor, and C.S. Lim: *Addit. Manuf.*, 2020, vol. 36, 101538.
25. Y. Gui, K. Aoyagi, and A. Chiba: *Mater. Sci. Eng. A*, 2023, vol. 864, 144595.
26. K. Aoyagi, H. Wang, H. Sudo, and A. Chiba: *Addit. Manuf.*, 2019, vol. 27, pp. 353–62.
27. Y. Gui, K. Aoyagi, H. Bian, and A. Chiba: *Addit. Manuf.*, 2022, vol. 54, 102736.
28. W.S. Noble: *Nat. Biotechnol.*, 2006, vol. 24, pp. 1565–67.
29. X. Huang, A. Maier, J. Hornegger, and J.A.K. Suykens: *Appl. Comput. Harmon. Anal.*, 2017, vol. 43, pp. 162–72.
30. H.C. Kim, S. Pang, H.M. Je, D. Kim, and S.Y. Bang: *Pattern Recognit.*, 2003, vol. 36, pp. 2757–67.
31. T.S. Furey, N. Cristianini, N. Duffy, D.W. Bednarski, M. Schummer, and D. Haussler: *Bioinformatics*, 2000, vol. 16, pp. 906–14.
32. G. Chen, S.Y. Zhao, P. Tan, J. Wang, C.S. Xiang, and H.P. Tang: *Powder Technol.*, 2018, vol. 333, pp. 38–46.
33. Q. Liu and N. Hansen: *Scr. Metall. Mater.*, 1995, vol. 32, pp. 1289–95.
34. J.B. Vogt, J. Bouquerel, F. Léaux, and F. Palleschi: *Procedia Eng.*, 2013, vol. 66, pp. 608–14.
35. A.G. Devendra Yadav: *Int. J. Mech. Eng.*, 2015, vol. 4, p. 5.
36. S. Sugawa, N. Tsutsumi, and K. Oda: *IOP Conf. Ser. Mater. Sci. Eng.*, 2018, vol. 372, p. 12008.

**Publisher's Note** Springer Nature remains neutral with regard to jurisdictional claims in published maps and institutional affiliations.